Ambipolar ion pumping with ratchet-driven active membranes

Alon Herman⬤ and Gideon Segev⬤*

School of Electrical Engineering, Tel Aviv University, Tel Aviv 6997801, Israel

In recent years there has been significant progress in the development of artificial ion-pumping membranes. Ion pumps based on asymmetric nanopores have been shown to operate as ionic current rectifiers, thus pumping a net ion flux against a concentration gradient even when driven with unbiased ac signals. However, since ion transport relies on charged nanopores, it is selective to either cations or anions, and thus cannot pump both cations and anions simultaneously. In this paper, we present a model for an electronically active membrane which is based on a *flashing* ratchet mechanism. The model includes adjacent electrolyte reservoirs and ion-ion interactions, which were not accounted for in prior similar models, and thus provides a better understanding of the driving mechanism and potential capabilities and limitations. It is shown that, unlike most other proposed ion pumps, the ratchet-based ion pump (RBIP) drives both cations and anions in the same direction and up a concentration gradient. This process, referred to as *ambipolar* ion pumping, is shown to be highly robust for many electrolyte compositions and input signals. The membrane is composed of alternating conductive thin layers (electrodes), separated by insulating layers in an asymmetric design. With insulating layer thicknesses of 70 and 30 nm and an input signal amplitude of 0.5 V, the device drives a salt flux of 0.03 mol/(m^2 s) in a mildly saline solution (10 mM). Thus, RBIPs may pave the way for many exciting future applications involving ambipolar ion pumping, most notably for desalination.

I. INTRODUCTION

Ion pumps can be found in any living cell membrane and are essential to many biological processes [1,2]. Because of their wide applicability, various approaches were taken towards the realization of artificial ion pumps [3]. For example, devices that pump ions with loading-unloading cycles using chemically gated membranes [4,5], light-driven proton pumps with photoacid-dye-sensitized membranes [6,7], or membranes doped with spiropyrans [8]. Ion pumps based on membranes with spatially asymmetric nanopores (such as conical nanopores) have gained significant interest in recent years [9–12]. In these membranes, surface-charged nanopores function as ionic current rectifiers, and the transmembrane potential is controlled by external electrodes. When the transmembrane potential is alternated, the rectified ion transport results in ion pumping even if the input signal is unbiased. Since the nanopore walls are charged, there is an excess of counterions in the channel, making the membrane selective for either cation or anion transport. Gated nanoporous membranes can potentially be used for *ambipolar* ion pumping (i.e., driving both cations and anions in the same direction) or water pumping by alternating their surface charge and therefore their ion selectivity [13–16].

An electric ratchet is a device that utilizes a temporal modulation of a spatially asymmetric electric potential to drive a steady-state flux of charged particles [17,18]. Ion pumps based on asymmetric nanopores could be viewed as *tilting* (or *rocking*) ratchets, where the asymmetric potential profile within the nanopores is "tilted" by an externally applied electric field [10,19]. As such, they are driven with external electrodes and the membrane itself does not provide a driving force for charge transport. In *flashing* ratchets, the potential profile within the nanopores is directly controlled and does not require external driving electrodes. Moreover, since potential gradients are applied to electrodes embedded within the membrane at short distances from each other (compared with the Debye length), it is possible to maintain high electric fields along the nanochannels with minimal Ohmic losses and without energetically expensive electrochemical reactions.

The use of flashing ratchets for ion transport was only recently suggested theoretically [20–22] and demonstrated experimentally [23]. Theoretical studies have shown that flashing ratchets have unique capabilities for tunable ion-ion selectivity [21,22], and potentially a higher energetic efficiency than reverse osmosis for nanofiltration [20]. Prior modeling of ion-pumping flashing ratchet systems assumed an ideal system in the sense that the potential distribution was predetermined, and ion-ion interactions were

not taken into consideration. Furthermore, fluctuations in the reservoirs of the electric potential and ion concentration were not accounted for [20,24]. Ratschow *et al.* simulated a gated conical nanopore with alternating bias [16]. Under some conditions this device can be described as a flashing ratchet; however, the authors focused on water flow through the device and questions related to its ion pumping performance were not addressed.

Here we present a computational study on the performance of an electrically active membrane, driven with a flashing ratchet mechanism in an electrolytic environment. The simulation accounts for the essential transport mechanisms, the Coulombic interaction between ions, and the effect of the potential and ion distribution in the adjacent reservoirs. The suggested membrane structure consists of alternating electrically conductive and insulating thin layers. The possibility of fabricating such multilayered structures using conventional thin-film deposition techniques provides great promise for achieving different electric potential landscapes within a solution. The specific design presented here, which creates a sawtooth-shaped potential, is the simplest ratchet profile that could be realized with the layered design. However, this structure could plausibly be expanded with additional layers to create a more complex ratchet class, called a *reversible* ratchet, that could potentially transport ions at a very high efficiency [25].

II. SIMULATION DETAILS

Figure 1(a) shows a schematic illustration of an RBIP membrane placed between two electrolyte reservoirs. The ratchet-based ion pump (RBIP) is constructed from three thin electrically conductive layers through which a time-dependent voltage signal $V_{\text{in}}(t)$ is applied, according to the scheme. Separating the conducting layers are two insulating layers with different thicknesses; thus, when a voltage is applied, an asymmetric potential distribution within the nanochannel is obtained. To reduce the computational burden, the RBIP performance is simulated using a one-dimensional model, as shown in Fig. 1(b). This simplified model can describe the device performance adequately under the following assumptions: (i) the diameter of the nanochannels is similar to the Debye length in the electrolyte (i.e., minimal potential decay towards the center of the nanochannel); (ii) the density of the nanochannels in the membrane is sufficiently large, so that the effective reservoir diameter is close to the nanochannel diameter. The simplified model also serves as a first step that provides basic mechanistic information prior to examining a more complex three-dimensional model. Furthermore, the conducting layers (electrodes) are modeled as points (zero-dimensional) and are assumed to be ideally polarizable (no Faradaic reactions). The walls of the nanochannels through the insulating layers are assumed
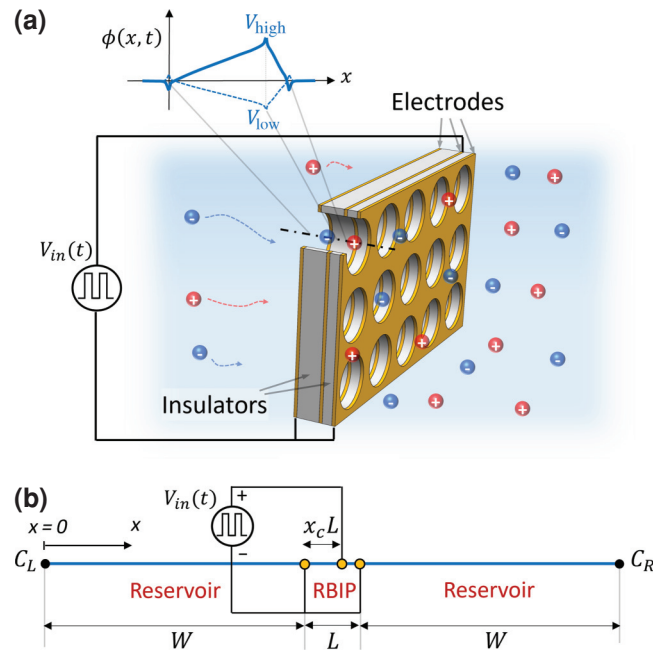

FIG. 1. (a) An illustration of the RBIP membrane acting between two electrolyte reservoirs. The device is constructed from three thin electrically conducting layers (electrodes), through which a time-dependent voltage signal $V_{\text{in}}(t)$ is applied, and two insulating layers between them with different thicknesses. Thus, an asymmetric potential distribution is induced within the nanochannel. (b) A one-dimensional model of the system.

to be uncharged. Lastly, solvent convection is not considered. Although electro-osmotic (solvent) flux is largely constrained for small nanochannels (assuming no slip at the nanochannel walls) [26], it is difficult to predict its effects on the device's performance, especially at high voltages and small interelectrode distance. Therefore, a more detailed account of convection effects (by coupling the Navier-Stokes equations) is left for future work.

The layered RBIP device has a total thickness L, and the reservoirs' length scale is W (assumed to be much larger than the Debye length). The ratchet symmetry factor x_c determines the relative position of the middle electrode, and it is defined as the ratio between the thickness of the left insulator and the total ratchet thickness. The distribution of the electric potential, and of the cations and anions (and their ionic current), in response to an input signal are found by solving the one-dimensional Poisson-Nernst-Planck (PNP) equations using COMSOL Multiphysics® v6.1. Assuming a symmetric binary $z:z$ electrolyte, no solvent convection, and no bulk reactions, the governing equations are as follows:

$$-\varepsilon \frac{\partial^2 \phi}{\partial x^2} = Fz(C_+ - C_-),   \tag{1}$$

$$\frac{\partial C_\pm}{\partial t} = -\frac{\partial J_\pm}{\partial x} = -\frac{\partial}{\partial x}\left(-D_\pm\frac{\partial C_\pm}{\partial x} \mp \frac{zD_\pm}{V_{\text{th}}}C_\pm\frac{\partial \phi}{\partial x}\right),$$

$$(2)$$

where ϕ is the electrical potential in the solution, z is the ion valence, $V_{\text{th}} = RT_r/F$ is the thermal voltage, and C_+ and C_- are the cation and anion concentrations, respectively. $J_\pm$ and $D_\pm$ are the cation and anion flux and diffusion coefficient, respectively. ε, F, R, and T_r are the dielectric permittivity of the solvent, Faraday's constant, universal gas constant, and the temperature, respectively.

The boundary conditions of the potential determine how the ratchet is electrically driven. The input signal is applied to the middle electrode, relative to the left and right electrodes. In addition, a reference point for the potential is defined at the left edge of the system ($x = 0$) and the right edge of the system is defined as electrically insulating. Since the signal is electrically floating (with respect to the bulk solution in both reservoirs), there is no electric double layer (EDL) formed at the reference point. Hence, the boundary conditions for the potential can be formulated as

$$\phi(x = W + x_c L, t) - \phi(x = W, t) = V_{\text{in}}(t), \quad (3)$$

$$\phi(x = W, t) = \phi(x = W + L, t), \quad (4)$$

$$\phi(x = 0, t) = 0, \quad (5)$$

$$\partial\phi/\partial x(x = 2W + L, t) = 0. \quad (6)$$

More information on the electric potential boundary conditions is given in the Supplemental Material [27]. The input signal $V_{\text{in}}(t)$ is a periodic square wave signal that is defined for some integer time period n as follows:

$$V_{\text{in}}(t) = \begin{array}{ll} V_{\max}, & nT < t < (n + \delta)T \\ \alpha V_{\max}, & (n + \delta)T < t < (n + 1)T \end{array}. \quad (7)$$

Each time period is described by a duty cycle $\delta = \tau_1/T$, which is the ratio between the duration of the first step τ_1, where the potential is at its maximum value $V_{\max}$, to the total duration $T(= 1/f)$. The time period is completed with a second step in which the potential is multiplied by a potential symmetry factor in the range $-1 \leq \alpha \leq 0$. The variable $\tau = t - nT$ is defined within each time period and is set to zero at the beginning of each period.

Electroneutrality is maintained at the outer edges of the reservoirs since W is much larger than the Debye length. Thus, we can define the ion concentration at the outer edge of the left reservoir as $C_L(t) = C_\pm(x = 0, t)$, and at the outer edge of the right reservoir as $C_R(t) =$ $C_\pm(x = 2W + L, t)$. The net ion flux at some time period n is defined as

$$J_{\pm,\text{net}}(x, nT) = (1/T)\int_0^T J_\pm(x, nT + \tau)d\tau. \quad (8)$$

For convenience, some of the variables are normalized such that $\tilde{t} = t/T$, $\tilde{\tau} = \tau/T$, $\tilde{x} = x/L$, $\tilde{C} = C/C_0$, and $\tilde{J}_\pm = J_\pm/(D_\pm C_0/W)$, where C_0 is the bulk electrolyte concentration.

Two types of systems are simulated. The first is a *closed system* where the ionic fluxes are set to zero at the reservoir outer edges, i.e., $J_\pm(x = 0, t) = J_\pm(x = 2W + L, t) = 0$. The initial conditions are $\phi(x, 0) = 0$ and $C_\pm(x, t = 0) = C_0$. Since the flux is zero at the outer edges of the domain, the net ion flux between the reservoirs is calculated according to the change in concentration at the outer edges. More details on the net flux calculation in the closed system can be found in the Supplemental Material [27]. Each simulation is run until the per-period average ion concentration at the reservoirs' outer edges reaches a steady state. At this point the average ion flux (over a time period) is zero. Since the total amount of ions in the system is constant, this type of system allows us to follow changes in ion concentrations between the reservoirs over time. In the second type of system, termed an *open system*, a constant bulk concentration boundary condition is set at the reservoir edges, such that $C_L = C_0$ and $C_R \geq C_L$. Each simulation is run until the per-period average ion flux at the reservoirs' outer edges reaches a steady state. Owing to the constant concentrations at the outer edges, a nonzero steady-state flux can be achieved, and the pumping performance of the device can be analyzed as a function of C_R/C_L. The initial conditions for the open system and additional simulation definitions are given in the Supplemental Material [27].

III. RESULTS AND DISCUSSION

A. RBIP operation in a closed system

Figure 2 shows the RBIP operation in a closed system. The ratchet thickness is $L = 100$ nm, the symmetry factor is $x_c = 0.7$, and the reservoirs' lengths are $W = 5L$. The initial concentration is $C_0 = 1$ mM (which corresponds to Debye length $\lambda_D \cong 10$ nm, at room temperature). The input $V_{\text{in}}(t)$ is a symmetric square wave signal with $V_{\max} = 0.5$ V, $\alpha = -1$, $\delta = 0.5$, and $f = 1$ MHz. Figure 2(a) shows the net salt flux ($J_+ = J_-$) and the changes over time of the ion concentration at the right and left edges of the reservoirs. The electrolyte is symmetric with diffusion coefficients of $D_\pm = 2 \times 10^{-9}$ m^2/s, and ion valence $z = 1$. Figure 2(b) shows the same for NaCl solution, which corresponds to $D_{\text{Na}^+} = 1.33 \times 10^{-9}$ m^2/s and $D_{\text{Cl}^-} = 2.03 \times 10^{-9}$ m^2/s. In both cases the net transport is ambipolar, i.e., the ratchet is driving cations and anions in the same direction. Since the flux is positive, the
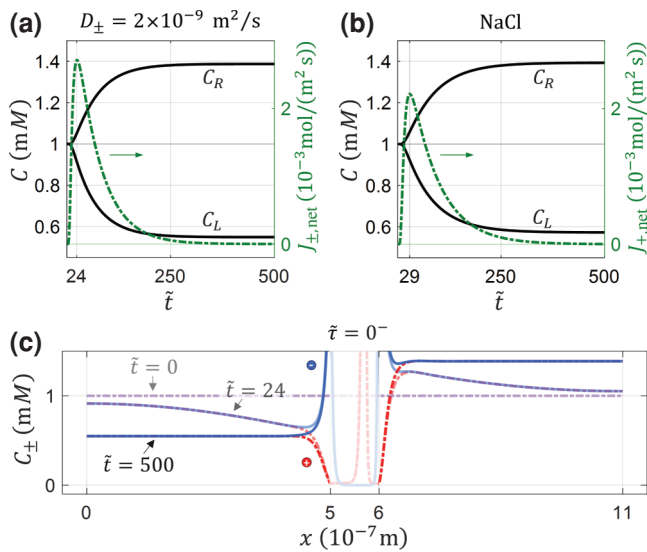
FIG. 2. RBIP operation in a *closed system*. Ion concentration over time at the right and left edges of the reservoirs (solid black lines, left y axis), and the net salt flux (dot-dash green line, right y axis), for a binary electrolyte ($z = 1$) with (a) symmetric diffusion coefficients, $D_{\pm} = 2 \times 10^{-9}$ m²/s, and (b) NaCl ($D_{Na^+} = 1.33 \times 10^{-9}$ m²/s and $D_{Cl^-} = 2.03 \times 10^{-9}$ m²/s). (c) Spatial concentration distribution of the cations (dot-dash red line) and anions (solid blue line) for $D_{\pm} = 2 \times 10^{-9}$ m²/s. The region inside the membrane ($5 \times 10^{-7} < x < 6 \times 10^{-7}$ m) is faded-out for visual clarity. The distributions are shown right before the switch to a positive potential, $\tilde{\tau} = 0^-$, and for different time periods during the process. System parameters: $L = 100$ nm, $x_c = 0.7$, $W = 5L$, $C_0 = 1$ mM, $V_{max} = 0.5$ V, $\alpha = -1$, $\delta = 0.5$, and $f = 1$ MHz.

ion concentration in the left reservoir decreases, while the concentration in the right reservoir increases. The concentration gradient that is built between the reservoirs opposes the ratchet operation, until finally at $\tilde{t} \sim 300$ the concentration at both edges reaches a steady state. The net flux reaches a maximum at $\tilde{t} = 24$ for the symmetric electrolyte and $\tilde{t} = 29$ for NaCl [Figs. 2(a) and 2(b), respectively], and then gradually declines until it reaches zero at $\tilde{t} \sim 300$ when the ratchet drive is balanced by the concentration gradient between the reservoirs. The overall behavior and steady-state concentration ratio C_R/C_L of the symmetric electrolyte and NaCl are very similar. However, in NaCl, sodium has a lower diffusion coefficient than chloride, and as a result, Coulombic interaction will impede the chloride transport. This leads to a lower salt flux and slightly longer time to reach steady state [Fig. 2(b)]. Owing to a net accumulation of ions in the ratchet area, the total number of ions that are added to the right reservoir is slightly smaller than the number of ions that are extracted from the left reservoir [Figs. 2(a) and 2(b)]. This effect becomes negligible for larger reservoir volumes. Figure 2(c) shows the spatial concentration distribution of the cations (dot-dash red line) and anions (solid blue line), for $D_{\pm} = 2 \times 10^{-9}$ m²/s

[same conditions as Fig. 2(a)]. The region inside the membrane ($5 \times 10^{-7} < x < 6 \times 10^{-7}$ m) is faded-out for visual clarity. The distributions are shown right before the switch to a positive potential ($\tilde{\tau} = 0^-$) for different time periods during the process. At the initial state ($\tilde{t} = 0$), the concentration of the ions is uniform everywhere in the domain, thus $C_{\pm} = C_0$. At $\tilde{t} = 24$, where the flux is maximal, the ratchet extracts ions from the left reservoir and transports them to the right reservoir. Eventually the system reaches a steady concentration difference between the reservoirs, as shown for $\tilde{t} = 500$. At this point the net flux is zero since the ratchet operation is completely negated by the concentration difference. Although not trivial, net ion transport is obtained here with an unbiased potential input (i.e., $\alpha = -1$, $\delta = 0.5$), which is in line with previous findings of Brownian pumps [28].

B. RBIP transport mechanism

To study the transport mechanism of the RBIP, we analyze the temporal changes in electric potential, ion concentration, and ion flux, during a time period in steady state, as shown in Fig. 3. The term steady state here refers to a state in which the initial condition of the device no longer affects its output. The device geometry and all system parameters are as in Fig. 2(a), except the frequency, which is $f = 100$ kHz. An open system is used with no concentration gradient between the reservoirs ($C_R = C_L = 1$ mM). Figure 3(a) shows snapshots of the ratchet region at a few key times in the period. The electric potential is illustrated by the dotted black line (left vertical axis). At $\tilde{\tau} = 0^-$, just before the first potential switch, cations (dot-dash red line, right vertical axis) are accumulated at the potential minimum induced by the middle electrode, and anions (solid blue line, right vertical axis) are accumulated at the left and right electrodes, which are the potential maxima. Focusing first on the anions in the right section of the ratchet and right reservoir, shortly after the switch ($\tilde{\tau} = 0.0025$) most anions drift towards the middle electrode; however, there is a small subset of anions that remain in the right reservoir. The blue shaded area marks this group, and it consists of all the anions in the right reservoir that are in excess of the baseline (steady-state) distribution (reached at $\tilde{\tau} = 0.5$). In the time interval $0.03 < \tilde{\tau} < 0.5$, most of those anions diffuse to the right. This is because they face a local potential barrier at the right electrode (approximately $5 - 5.6\ V_{th}$), while towards the bulk of the right reservoir there is no opposing electric field. In the second half of the period ($0.5 < \tilde{\tau} < 1$), the anions that accumulated near the middle electrode split into two groups, with the majority drifting back towards the right electrode. It is found that more anions are transported back to the right electrode than were extracted from it in the first half of the period. The difference is exactly the number of ions that were transported to the right reservoir in the first part of the cycle. We note
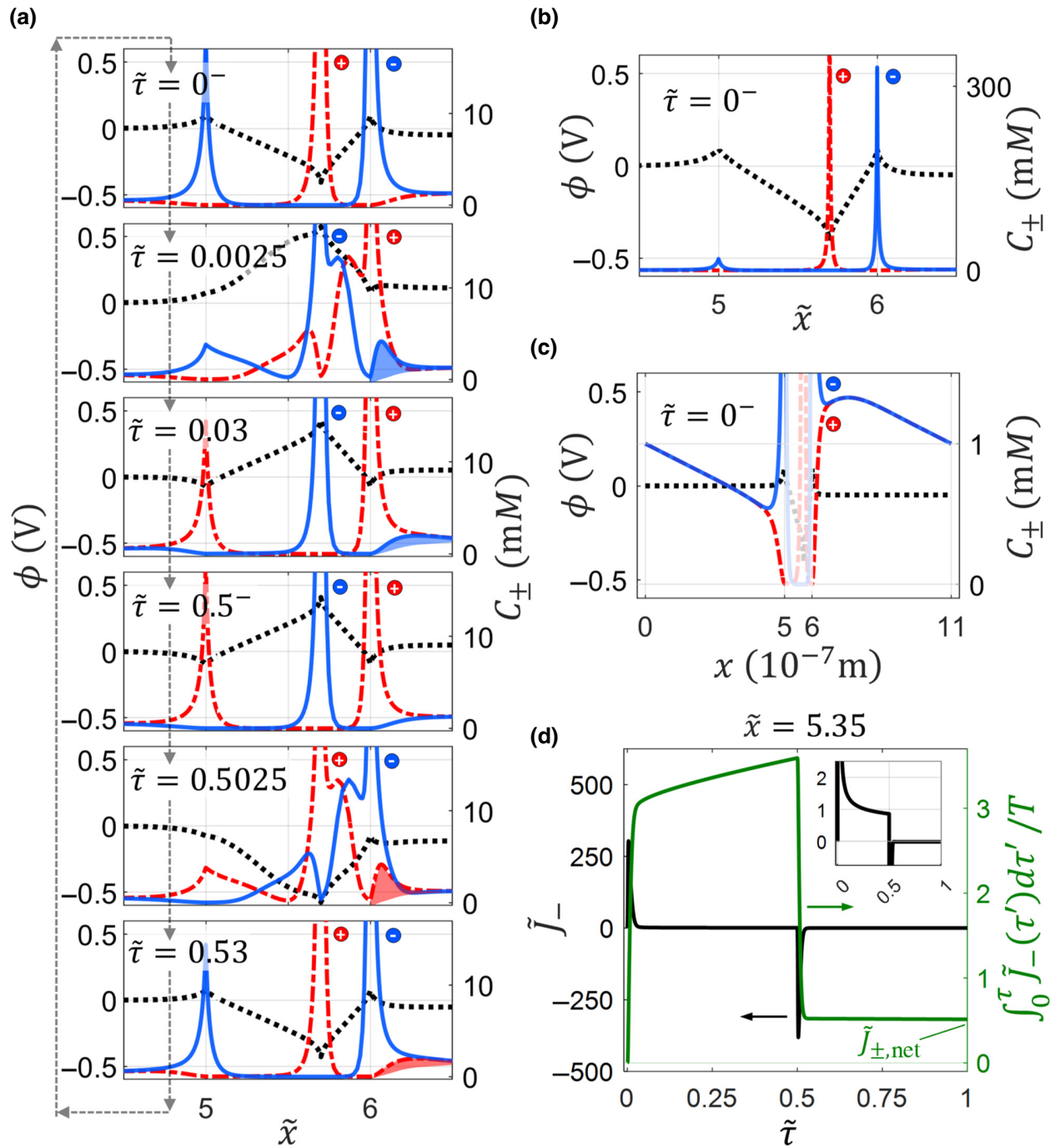
FIG. 3. Analysis of the RBIP transport mechanism. (a) Enlarged view of the spatial distribution of cations (dot-dash red line), anions (solid blue line), and electric potential (dot-dot black line), at a few key times during a period. Shaded areas represent ions that are diffusing to the right reservoir. The same results are presented in (b) showing the peak concentration at the electrodes, and in (c) for the full x axis, showing the distribution in the reservoirs. The region inside the membrane ($5 \times 10^{-7} < x < 6 \times 10^{-7}$ m) is faded-out for visual clarity. (d) Normalized anion flux $\tilde{J}_-$ inside the membrane at $\tilde{x} = 5.35$ (left y axis), and the integral of $\tilde{J}_-$ up to point τ along a time period (right y axis). The inset shows the same data focusing on the slower current components. Results are for an *open system* in steady state. System parameters: $L = 100$ nm, $x_c = 0.7$, $W = 5L$, $D_\pm = 2 \times 10^{-9}$ m^2/s, $C_0 = 1$ mM, $C_R/C_L = 1$, $V_{\max} = 0.5$ V, $\alpha = -1$, $\delta = 0.5$, and $f = 100$ kHz.

that in the first half period, there is also a small subset of anions that remain in the left reservoir. However, because of the spatial asymmetry, the potential barrier at the left electrode is much smaller than it is in the right electrode (approximately $2.9 - 3.7 \, V_{th}$ between $0.03 < \tilde{\tau} < 0.5$). As a result, diffusion towards the left reservoir is much less pronounced compared with the diffusion process towards the right reservoir discussed previously. Hence, by $\tilde{\tau} = 0.5^-$, more anions from the left reservoir make their way to the middle electrode, then will go back to the left from the middle electrode in the second half of the period (see discussion in the next paragraph). Considering that anions and cations in this case have the same diffusivity and that the input signal is temporally symmetric, the same process described previously takes place for cations, with a shift in time of half a period. The result is a net flux of both anions and cations in the positive x direction. This is further exemplified in Fig. 3(c), in which the full length of the system is displayed. Far from the ratchet, the ion distribution is linear with a diffusion flux ($\propto \partial C / \partial x$) that is equal at both reservoirs.

Figure 3(d) shows the normalized anion flux $\tilde{J}_-$ at the center of the left ratchet section ($\tilde{x} = 5.35$) over the course of a time period at steady state (left y axis). It also shows the cumulative flux within a time period $\int_0^\tau \tilde{J}_-(\tau')d\tau'/T$ (right y axis). This value is the total contribution to the flux up to a point τ in the period. It is normalized by T, so the result at $\tau = T$ is exactly the net flux, $\tilde{J}_{\pm,net}$, which in steady state is equal everywhere in the system. Only the anion flux is shown; however, the net flux of anions and cations is equal. The flux peak between $\tilde{\tau} = 0$ and $\tilde{\tau} \sim 0.03$ corresponds to anions discharging from the left electrode, drifting along the left ratchet section, and charging the middle electrode. Between $\tilde{\tau} = 0.5$ and $\tilde{\tau} \sim 0.53$, there is an opposite negative flux peak due to anion motion back toward the left electrode. These fast back-and-forth transport events almost entirely cancel out in terms of their contribution to the net flux. The inset shows the normalized temporal flux focusing on the slower flux components. Although there is an initial sharp decline in its magnitude, the flux is not diminished by $\tilde{\tau} = 0.5$. This nonzero flux is comprised of anions from the left reservoir, which diffuse over the small potential barrier at the left electrode and then drift towards the middle electrode. This is also the reason for the moderate but overall significant increase in the cumulative flux between $0.03 < \tilde{\tau} < 0.5$. There is no opposite transfer of anions to the left between $0.53 < \tilde{\tau} < 1$ due to the large potential barrier at the middle electrode. Thus, the net flux through the left section of the ratchet is mostly a result of a relatively slow transport of ions from the left reservoir between $0.03 < \tilde{\tau} < 0.5$.

The last two paragraphs have described separately the process of ion transport from the left reservoir up to the middle electrode, and from the middle electrode to the right reservoir. The system reaches a steady state when the ion transport rate of both processes is equal. The underlying reason that allows both processes is ultimately derived from the spatial asymmetry of the device, which results in a higher ion concentration and larger potential barrier at the right electrode compared with lower ion concentration and smaller potential barrier at the left electrode, as shown for example at $\tilde{\tau} = 0^-$ in Fig. 3(b). Further discussion on this effect can be found in the Supplementary Material [27].

The potential distribution in the ratchet [$5 < \tilde{x} < 6$ in Fig. 3(a)] is close to a linear sawtooth at any point during the cycle since there is very little potential screening at the electrodes. This is partly explained by the potential switching times, which are too short for the system to reach the final ion distribution. However, this is not the main reason, since the signal frequency is not very large compared with the fast transport processes (after each potential switch). For example, potential screening does not become significant even for a signal frequency as low as 5000 Hz. Instead, it is mainly the result of the low total amount of ions available within the ratchet area, due to the small length scale of the device and the low bulk concentration. In other cases where the bulk concentration is higher or the device length scale is larger, such as presented in Fig. S1 in the Supplemental Material [27], potential screening is much more pronounced even at higher normalized frequencies. Nevertheless, as will be shown in the next section, minimal potential screening is neither a prerequisite nor is it necessarily an optimal condition for ion pumping.

Ambipolar transport was previously identified, but only for nonsymmetric electrolytes ($D_+ \neq D_-$) and a particular subset of input signals [22]. With the current model, which accounts for the Coulombic interaction between ions and reservoir effects, ambipolar transport is inherent and it is highly robust. It persists for symmetric [Figs. 2(a) and 3] and nonsymmetric electrolytes [Fig. 2(b)], as well as for time-symmetric [Figs. 2(a), 2(b), and 3] and non-time-symmetric input signals (see Fig. S2 in the Supplemental Material [27]). In ON-OFF ratchets, where $\alpha = 0$, ambipolar pumping is still achieved. However, due to counterion interactions, the net flux is much lower, and ion pumping is in the opposite direction to that predicted by other models [20,24].

The analysis in this section provides a general understanding of the different time scales that are involved in the temporal evolution of ionic flux. These time scales are consistent with the general dynamics of microelectrochemical systems [29]. They include fast processes occurring within the EDLs and slower processes within the bulk of the membrane and the reservoirs, which are associated with large applied voltages (relative to V_{th}). The overall operation of the device is a result of a complex interaction between these different processes, which may vary for different electrolyte compositions, system geometries, and input signals. The next section will examine the RBIP

performance as a function of a few key parameters of the system: the input signal frequency and amplitude, the ratchet geometry (device thickness and symmetry factor), and the bulk concentration.

C. RBIP performance analysis for key parameters

A few key parameters of the RBIP system are analyzed here to determine their effect on pumping performance. Figures 4(a) and 4(b) show the normalized net salt flux as a function of normalized signal frequency for different ratchet geometries and bulk concentrations when there is no concentration difference between the reservoirs ($C_R/C_L = 1$). The frequency is normalized by a characteristic time scale for each half of the period and is defined as $\tilde{f} = f/[D/(2L^2)]$. Each curve has an optimal frequency where the flux is maximal, which is expected in ratchet systems. Figures 4(c) and 4(d) show the normalized net salt flux as a function of the concentration ratio between the reservoirs C_R/C_L at specific signal frequencies. The x-axis intersection, marked $(C_R/C_L)_{\max}$, is the maximal concentration ratio that the ratchet can overcome (with zero flux), similar to an open-circuit voltage of a solar cell, or to a maximal pressure of a pump. The y-axis intersection, marked $\tilde{J}_{\max}$, is the maximal normalized net flux that is achieved when there is no opposing concentration difference, similar to a short-circuit current. At the operating points along the curve, the ratchet is performing work, i.e., it drives an ionic current up a concentration gradient. For comparison, a "No ratchet" curve is shown, which is calculated as the diffusion flux for a system of the same total length $2W + L$ and no ratchet present.

Figures 4(a) and 4(c) explore the pumping characteristics for a ratchet thickness of $L = 0.1\ \mu m$ and a bulk concentration $C_0 = 1\ mM$. For a spatial asymmetry of $x_c = 0.7$, driving the ratchet at the optimal normalized frequency $\tilde{f} = \tilde{f}_{opt} = 1$ (which corresponds to $f = 100$ kHz) results in a higher pumping performance than $\tilde{f} = 10$ ($f = 1$ MHz) for all concentration ratios. A larger asymmetry factor $x_c = 0.9$ results in a higher optimal frequency and significantly improved pumping performance for all concentration ratios. The last curve, denoted "Thick electrodes," is calculated assuming electrodes with a finite thickness of 10 nm. In this case, the input potential is applied on the thin electrodes' regions (not at points), and the ratchet thickness L and asymmetry factor x_c are based only on the insulators' size. The optimal frequency and pumping performance are somewhat reduced, but the overall behavior is similar.

For a ratchet thickness $L = 0.1\ \mu m$, when C_0 increases from 1 to 10 mM, the maximal normalized net flux increases by 40% [Fig. 4(b)], which corresponds to an absolute net flux increase by a factor of 14. Part of this increase in absolute flux is due to the tenfold rise in
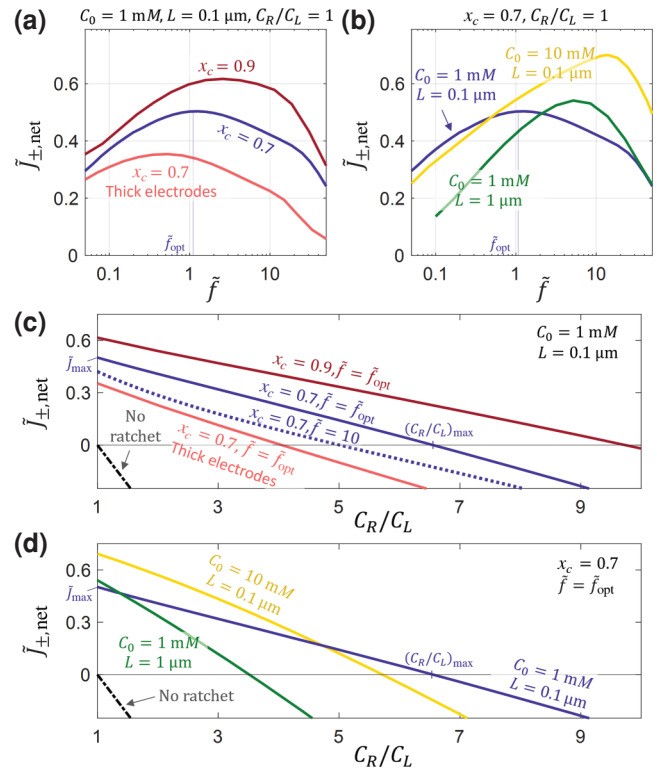

FIG. 4. RBIP performance analysis for different frequencies, ratchet geometries, and bulk concentrations. Normalized net salt flux as a function of (a), (b) normalized signal frequency when $C_R = C_L$, and (c), (d) opposing concentration ratio. General system parameters: $W = 5L$, $D_\pm = 2 \times 10^{-9}$ m^2/s, $C_L = C_0$, $V_{\max} = 0.5$ V, $\alpha = -1$, $\delta = 0.5$. The PNP equations are valid for frequencies near and above the optimal frequency of each presented case.

bulk concentration, but the additional increase in normalized flux for $C_0 = 10$ mM is due to a larger fraction of ions (with respect to the bulk concentration) being transferred across the membrane in each time period. This fraction is larger for $C_0 = 10$ mM at any specific frequency above $\tilde{f} = 0.5$, and especially for $\tilde{f} > 10$, as shown in Supplemental Material Fig. S3 [27]. An analogy can be drawn between this and a simple RC circuit, where a higher bulk concentration results in faster transients ($\tau_{RC} = R_b C_D \propto 1/\sqrt{C_0} \propto \lambda_D$, where R_b is the bulk electrolyte resistance, and C_D is the double-layer capacitance), which enables operation at higher frequencies. Figure 4(d) shows that the maximal concentration ratio for $C_0 = 10$ mM is slightly lower than for $C_0 = 1$ mM. However, the maximum normalized output power, which is found by $[\tilde{J}_{\pm,\mathrm{net}} \ln(C_R/C_L)]_{\max}$, is higher by 35% for $C_0 = 10$ mM. The RBIP's ability to pump both cations and anions against a concentration gradient at moderate salinity levels implies that it can be suitable for brackish water desalination. To achieve the required concentration gradients, a multistage process may be needed. A detailed

analysis of the pumping efficiency and comparison to other desalination methods is left for future work.

The PNP equations do not consider steric effects [30]. Thus, for larger bulk concentrations, and relatively low signal frequencies, the peak concentration at the electrodes might exceed realistic values. However, it was verified that the ion concentration near (and above) the optimal frequency does not exceed the steric limit (calculated to be $4.8M$, assuming an effective ion size of 7 Å for both cations and anions [30]). The performance of the device is highly dependent on the charging-discharging properties of the EDLs, which are in turn highly affected by steric effects near the electrodes. It was also shown that under relatively large voltages, the charging-discharging behavior of the EDLs is nonmonotonic with voltage amplitude [30]. Therefore, predicting the impact of steric effects at higher salinities and/or lower frequencies is not trivial and will require further investigation that is beyond the scope of this work.

Figures 4(b) and 4(d) also show curves for a device with a ratchet thickness of $L = 1 \ \mu$m and a bulk concentration $C_0 = 1$ mM. A larger length scale requires a longer ion transport time, which naturally results in a lower optimal frequency $f_{opt} = 5$ kHz ($\tilde{f}_{opt} = 5$). This also leads to a lower (absolute) net salt flux compared to a smaller ratchet thickness. The potential distribution and ion concentration for such a device, working at the optimal frequency, are shown in Supplemental Material Fig. S1 [27]. Unlike the 0.1-μm-thick device, here the total number of ions within the membrane is sufficient to completely screen the applied potential (except for very short durations shortly after potential switches). Nevertheless, the normalized pumping performance is only somewhat reduced, resulting in a lower maximal concentration ratio, and the overall transport mechanism is similar to that shown in Fig. 3. Supplemental Material Fig. S4 [27] compares the operation of this device ($L = 1 \ \mu$m, $C_0 = 1$ mM) to a device with the same ratio of λ_D/L, i.e., a ratchet thickness $L = 0.1 \ \mu$m and a bulk concentration $C_0 = 100$ mM. Although the absolute net flux and operational frequency range vary by orders of magnitude between the cases, the normalized curves perfectly coincide. This demonstrates the key importance of this ratio to the device pumping characteristics. For $C_0 = 100$ mM the steric concentration limit is exceeded even near and above the optimal frequency, thus this result only serves to exemplify the effect of the λ_D/L ratio. Perhaps contrary to intuition, the best pumping performance is not obtained when the Debye length approaches the length scale of the device L (i.e., when potential screening by the electrolyte is negligible), but there is an optimal λ_D/L value, which can be much smaller than 1. For the ratchet parameters in Figs. 4(b) and 4(d), the optimal ratio is in the range $0.1 < (\lambda_D/L)_{opt} < 0.01$. Thus, when designing a device, it is important to consider that, although a smaller ratchet thickness L increases the net (absolute) salt flux, it also increases λ_D/L, which might somewhat reduce the pumping efficiency.

Consideration should be given to the optimal frequency (at which the net ion flux is greatest). Predicting the optimal frequency for different ratchet geometries and bulk concentrations is not trivial. There are multiple time scales governing ion transport, and they depend on the length of the different sections in the system, and on the Debye length ($\propto 1/\sqrt{C_0}$) [29]. It also varies as a function of input signal amplitude V_{max}. Figure 5(a) shows the calculated net salt flux as a function of the input signal frequency for several input signal amplitudes. Figure 5(b) shows the number of moles transferred across the membrane per time period, $J_{\pm,net}/f$, calculated with the same data. For $V_{max} = 0.05$ V and $V_{max} = 0.1$ V, at the lower frequencies up to approximately 100 kHz, $J_{\pm,net}/f$ is almost constant since the system reaches equilibrium between each potential switch. Increasing the ratchet frequency leads to more transport cycles per unit time, thus resulting in a linear increase in net flux. As the frequency increases above approximately 100 kHz, $J_{\pm,net}/f$ starts to decrease. However, since this decrease is moderate at first, the contribution of the added transport cycles with frequency is more dominant and thus the net flux continues to increase. The optimal frequency is achieved at the point where the decrease in $J_{\pm,net}/f$ starts to outweigh the contribution of the added transport cycles. On the log-log graph in Fig. 5(b), this is equivalent to a slope that is more negative than -1. As V_{max} increases, $J_{\pm,net}/f$ also increases, and as a result so does the net flux. Interestingly, the optimal frequency decreases as a function of voltage amplitude. This may seem surprising at first since larger electric fields lead to faster ion transport, and indeed this is the case for the initial response of the system to each potential switch. However, when high voltages are applied (relative to V_{th}), the slower transport processes become more dominant (as discussed in Sec. III B). This results in longer times to reach equilibrium, and a significant increase in $J_{\pm,net}/f$ at the lower frequencies, which thereby reduces the optimal frequency. Fig. S5 in the Supplemental Material [27] shows the maximal net flux (for $C_R/C_L = 1$) and the maximal concentration ratio $(C_R/C_L)_{max}$ as a function of V_{max} for $f = 100$ kHz. The net flux increases as the effects of long-time-scale transport processes become more and more significant, until they reach saturation above $V_{max} = 0.4$ V. The maximal concentration ratio follows a similar trend, except the increase with amplitude only starts to become more moderate at $V_{max} = 0.4$ V. Owing to steric concentration limits, a study of the effects of higher signal amplitudes is left for future work. The increase of the maximum flux and $(C_R/C_L)_{max}$ with V_{max} and their saturation at a higher voltage implies that there is an amplitude for which the pumping efficiency is optimal. Since the
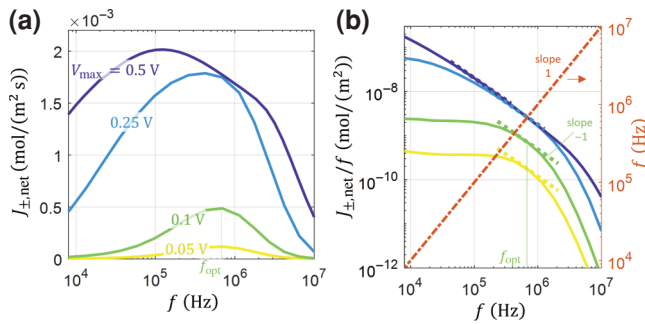
FIG. 5. Net salt flux, $J_{\pm,\text{net}}$ (a), and moles transported per time period, $J_{\pm,\text{net}}/f$ (b), as a function of signal frequency for different signal amplitudes. The dotted lines in (b) show the slope (in log-log) of the curves at the optimal frequency, and for reference the curve $f = f$ (right y axis, dash-dot line). General system parameters: $L = 0.1$ μm, $x_c = 0.7$, $W = 5L$, $D_\pm = 2 \times 10^{-9}$ m^2/s, $C_0 = 1$ mM, $C_R/C_L = 1$, $\alpha = -1$, $\delta = 0.5$.

thermodynamics of this process are out of the scope of this work, a detailed examination of this effect is left for future study.

An additional local frequency optimum may exist for nonsymmetric electrolytes ($D_+ \neq D_-$) when using input signal parameters that were shown to produce ambipolar transport (in a ratchet model that does not account for Coulombic interactions) [22]. For example, Fig. S6 in the Supplemental Material [27] shows the case for NaCl. It can be seen that there is a local increase in net flux compared to a symmetric electrolyte ($D_\pm = 2 \times 10^{-9}$ m^2/s) under the same conditions. As predicted by the noninteracting model, at the local frequency optimum, cations and anions are simultaneously driven in the same direction and with the same velocity, therefore reducing the impeding effect of Coulombic interactions within the membrane.

IV. CONCLUSIONS

We simulate the performance of an electrically activated RBIP membrane in an electrolytic environment accounting for Coulombic interaction between ions. The study shows that this device drives both cations and anions in the same direction (ambipolar pumping or salt pumping) and up a concentration gradient. This finding is highly robust for many electrolyte compositions and input signals. The results show that with an input signal amplitude of 0.5 V, the RBIP can pump ions against opposing concentration ratios as high as 10:1 without the need for electrochemical reactions at the electrodes. This work is a first step in the study of multilayered RBIPs, and it provides the basis for understanding the ambipolar pumping mechanism and its possible applications. The multilayered architecture holds great promise for fabricating membranes that can realize

different electric potential landscapes within a solution, potentially enabling high-efficiency water desalination.

[1] T. Y. Tsong and R. D. Astumian, Electroconformational coupling and membrane protein function, Prog. Biophys. Mol. Biol. **50**, 1 (1987).

[2] E. Gouaux and R. MacKinnon, Principles of selective ion transport in channels and pumps, Science **310**, 1461 (2005).

[3] T. Mei, H. Zhang, and K. Xiao, Bioinspired artificial ion pumps, ACS Nano **16**, 13323 (2022).

[4] H. Zhang, X. Hou, L. Zeng, F. Yang, L. Li, D. Yan, Y. Tian, and L. Jiang, Bioinspired artificial single ion pump, J. Am. Chem. Soc **135**, 16102 (2013).

[5] S. Benavides, S. Qu, F. Gao, and W. A. Phillip, Polymeric ion pumps: Using an oscillating stimulus to drive solute transport in reactive membranes, Langmuir **34**, 4503 (2018).

[6] W. White, C. D. Sanborn, D. M. Fabian, and S. Ardo, Conversion of visible light into ionic power using photoacid-dye-sensitized bipolar ion-exchange membranes, Joule **2**, 1 (2017).

[7] W. White, C. D. Sanborn, R. S. Reiter, D. M. Fabian, and S. Ardo, Observation of photovoltaic action from photoacid-modified Nafion due to light-driven ion transport, J. Am. Chem. Soc. **139**, 11726 (2017).

[8] X. Xie, G. A. Crespo, G. Mistlberger, and E. Bakker, Photocurrent generation based on a light-driven proton pump in an artificial liquid membrane, Nat. Chem. **6**, 202 (2014).

[9] Z. Siwy and A. Fuliński, Fabrication of a synthetic nanopore ion pump, Phys. Rev. Lett. **89**, 198103 (2002).

[10] Z. Siwy and A. Fuliński, A nanodevice for rectification and pumping ions, Am. J. Phys. **72**, 567 (2004).

[11] C. C. Harrell, P. Kohli, Z. Siwy, and C. R. Martin, DNA - nanotube artificial ion channels, J. Am. Chem. Soc. **126**, 15646 (2004).

[12] J. Experton, X. Wu, and C. R. Martin, From ion current to electroosmotic flow rectification in asymmetric nanopore membranes, Nanomaterials **7**, 445 (2017).

[13] Y. Zhang and G. C. Schatz, Advantages of conical pores for ion pumps, j. phys. chem. c **121**, 161 (2017).

[14] Y. Zhang and G. C. Schatz, Conical nanopores for efficient ion pumping and desalination, J. Phys. Chem. Lett. **8**, 2842 (2017).

[15] M. Tagliazucchi and I. Szleifer, Salt pumping by voltage-gated nanochannels, J. Phys. Chem. Lett. **6**, 3534 (2015).

[16] A. D. Ratschow, D. Pandey, B. Liebchen, S. Bhattacharyya, and S. Hardt, Resonant nanopumps: ac gate voltages in conical nanopores induce directed electrolyte flow, Phys. Rev. Lett. **129**, 264501 (2022).

[17] V. M. Rozenbaum, T. Y. Korochkova, A. A. Chernova, and M. L. Dekhtyar, Brownian motor with competing spatial and temporal asymmetry of potential energy, Phys. Rev. E **83**, 051120 (2011).

[18] P. Hänggi and F. Marchesoni, Artificial Brownian motors: Controlling transport on the nanoscale, Rev. Mod. Phys. **81**, 387 (2009).

[19] B. Lau, O. Kedem, J. Schwabacher, D. Kwasnieski, and E. A. Weiss, An introduction to ratchets in chemistry and biology, Mater. Horizons **4**, 310 (2017).

[20] S. Marbach, N. Kavokine, and L. Bocquet, Resonant osmosis across active switchable membranes, J. Chem. Phys. **152**, 054704 (2020).

[21] S. Marbach and L. Bocquet, Active sieving across driven nanopores for tunable selectivity, J. Chem. Phys. **147**, 154701 (2017).

[22] A. Herman, J. W. Ager, S. Ardo, and G. Segev, Ratchet-based ion pumps for selective ion separations, PRX Energy **2**, 023001 (2023).

[23] R. J. Kautz, A. Herman, E. J. Heffernan, C. Muñetón, D. Larson, J. W. Ager III, F. M. Toma, S. Ardo, and G. Segev, A Nanoporous Capacitive Electrochemical Ratchet for Continuous Ion Separations, ArXiv: 2309.00951 (2023).

[24] A. Gomez-Marin and J. M. SaNcho, Two-state flashing molecular pump, EPL **86**, 40002 (2009).

[25] J. M. R. Parrondo, J. M. Blanco, F. J. Cao, and R. Brito, Efficiency of Brownian motors, Europhys. Lett. **43**, 248 (1998).

[26] D. G. Haywood, Z. D. Harms, and S. C. Jacobson, Electroosmotic flow in nano fluidic channels, Anal. Chem. **86**, 11174 (2014).

[27] See Supplemental Material at http://link.aps.org/supplemental/10.1103/PhysRevApplied.21.034056 for more details on the electric potential boundary conditions, net flux calculation for a closed system, initial conditions for an open system, additional simulation definitions, higher ion concentration at the right electrode, and Supplemental Material figures.

[28] V. M. Rozenbaum, Y. A. Makhnovskii, I. V. Shapochkina, S. Y. Sheu, D. Y. Yang, and S. H. Lin, Adiabatically driven Brownian pumps, Phys. Rev. E **88**, 012104 (2013).

[29] M. Z. Bazant, K. Thornton, and A. Ajdari, Diffuse-charge dynamics in electrochemical systems, Phys. Rev. E **70**, 021506 (2004).

[30] M. S. Kilic, M. Z. Bazant, and A. Ajdari, Steric effects in the dynamics of electrolytes at large applied voltages. I. Double-layer charging, Phys. Rev. E **75**, 021502 (2007).